Tuning Stability of AB₃-Type Alloys by Suppressing Magnetism

Hung Ba Tran,*,† Toyoto Sato,‡ Ryuhei Sato,¶ Hiroyuki Saitoh,§ Shin-ichi Orimo,*,†,‡ and Hao Li*,†

†Advanced Institute for Materials Research (WPI-AIMR), Tohoku University, Sendai,
Miyaqi 980-8577, Japan

‡Institute for Materials Research (IMR), Tohoku University, Sendai, Miyagi 980-8577,

Japan

¶Department of Materials Engineering, The University of Tokyo, Tokyo 113-8656, Japan §National Institutes for Quantum Science and Technology, Sayo-gun, Hyogo 679-5148,

Japan

E-mail: tran.ba.hung.a6@tohoku.ac.jp; shin-ichi.orimo.a6@tohoku.ac.jp; li.hao.b8@tohoku.ac.jp

Abstract

Hydrogen is a promising clean energy carrier, yet effective and reversible storage remains a major challenge. AB₃-type intermetallic alloys have emerged as promising candidates for solid-state hydrogen storage owing to their intermediate thermodynamic stability and rapid hydrogen uptake. However, optimizing both stability and gravimetric density has been hindered by competing thermodynamic and magnetic effects. Here, we present a systematic analysis of AB₃ compounds (A = Ca, Y, Mg; B = Co, Ni) and their ternary alloys $Ca_xY_yMg_{1-x-y}B_3$ (B = Co, Ni), combining first-principles calculations with Monte Carlo simulations. **Strikingly, we uncover a direct correlation** between formation energy and total magnetic moment that dictates alloy

stability, thereby explaining the observed trade-off in hydrogen storage optimization. In Co-based systems with large lattice volumes, such as Ca-rich and Y-rich compositions, formation energy increases monotonically with magnetization, exhibiting a near one-to-one correlation and establishing magnetism as the dominant factor governing alloy stability. While Mg-rich compositions achieve high gravimetric densities, strong magnetism destabilizes the system, necessitating Y substitution to suppress magnetic moments and stabilize a low-spin state—thereby limiting optimization when heavy Y is introduced. In contrast, replacing Co with Ni dramatically weakens the magnetism: YNi₃ is nonmagnetic, while CaNi₃ and MgNi₃ display only weak spin polarization, enabling thermodynamic stability across the entire compositional range. Notably, the experimentally known CaMg₂Ni₉ combines high theoretical capacity (~3.32 wt%) with good reversibility, and our calculations further identify the Mg-rich Ni-based region as an unexplored compositional domain that couples negative formation energies with the highest gravimetric densities (up to ~3.40 wt%). These findings establish magnetism as a fundamental thermodynamic variable controlling alloy stability and reveal magnetic suppression via transition-metal substitution as the key to overcoming the stability-capacity trade-off in AB₃-type hydrogen storage materials.

Keywords: Metal Alloy, Coherent Potential Approximation, Stability, Magnetic Properties, Hydrogen Storage

Introduction

Hydrogen represents a clean and sustainable energy carrier for automobiles and power generation, supporting the global transition toward a zero-emission society. ^{1–3} Green hydrogen enables efficient storage of renewable energy from solar and wind sources, which can then be utilized in fuel cell systems. ^{1,4,5} However, effective hydrogen storage remains one of the most critical challenges in establishing a practical hydrogen-based infrastructure. ^{6,7} At ambient conditions, hydrogen gas exhibits extremely low volumetric

energy density.⁶ High-pressure storage increases density but requires heavy, specialized tanks that reduce gravimetric efficiency.⁷ This limitation parallels those of electric vehicles, where heavy batteries constrain driving range.⁸ Meanwhile, liquid hydrogen demands cryogenic temperatures (20 K), imposing large energy costs for cooling.^{6,7,9}

Metal hydrides provide a promising alternative by achieving high volumetric and gravimetric densities under moderate conditions. 6,7 Light-element hydrides such as MgH₂ and CaH₂ offer high hydrogen-to-metal ratios (H/M = 2.0), but binary hydrides generally suffer from thermodynamic extremes: overly stable compounds require prohibitively high desorption temperatures, while unstable compounds absorb hydrogen only under impractically high pressures. 6,7,10 Transition-metal hydrides add complexity through magnetic effects, which can either stabilize or destabilize the system. 6,7 Consequently, most binary hydrides are unsuitable for practical, reversible storage. 6,7,10

Ternary intermetallic hydrides offer a balanced solution by combining intermediate thermodynamic stability with reversible hydrogen absorption and desorption. ¹¹ These systems are categorized into AB, AB₂, AB₃, A₂B₇, and AB₅ types, where A forms a stable hydride with strong hydrogen affinity and B forms an unstable hydride with low affinity. ¹¹ Among them, AB₃ alloys–including YCo₃, CaNi₃, and LaNi₃–crystallize in the rhombohedral $R\bar{3}m$ (PuNi₃-type) structure. ^{11,12} This structure may be viewed as a hybrid of two-thirds of an AB₂ unit (ZrV₂ Laves phase) and one-third of an AB₅ unit (LaNi₅, CaCu₅ type), ^{12,13} as illustrated in **Figure 1**. The theoretical H/M ratio of AB₃ hydrides reaches 1.75 (AB₃H₇), intermediate between AB₂ (H/M = 2.0) and AB₅ (H/M = 1.5). ^{11–13} Compared to AB₅ alloys, AB₃ compounds provide higher gravimetric density, while unlike AB₂ systems, they combine moderate stability with favorable catalytic activity, enabling rapid hydrogen uptake. ^{11,13} Their rhombohedral structure also offers multiple interstitial sites that may host additional hydrogen under pressure. ¹¹ Furthermore, their magnetic properties can be tuned through composition, offering a route to optimize both stability and storage capacity. ¹⁴

YCo₃ serves as a prototypical AB₃ alloy but suffers from limited gravimetric capacity due to the heavy yttrium atom. ^{13,14} Its compositional modification is experimen-

tally challenging, as stability and magnetism are highly sensitive to Co content. 13,14 Sato et al. demonstrated that partial substitution of Y with Mg in $Y_xMg_{1-x}Co_3$ (x=0.58,0.68) enables reversible hydrogen cycling with a gravimetric density of ~ 2.88 wt% at room temperature under 10 GPa pressure. 15 However, this composition approaches the intrinsic performance limit of Co-based systems due to strong spin-driven stabilization. 15 By contrast, Ni-based AB₃ alloys such as $Ca_xY_yMg_{1-x-y}Ni_3$ achieve reversible hydrogen storage with high stability, suggesting that Ni substitution may overcome the magnetically constrained optimization bottleneck of Co-based systems. $^{11,16-20}$ These advances underscore the urgent need for mechanistic insights into how magnetism controls thermodynamics and hydrogen storage performance.

In this work, we conduct a comprehensive analysis of stoichiometric AB₃ alloys (A = Ca, Y, Mg; B = Co, Ni) and their ternary solid solutions $Ca_xY_yMg_{1-x-y}Co_3$ and $Ca_xY_yMg_{1-x-y}Ni_3$. Chemical disorder is efficiently treated using the coherent potential approximation (CPA) within first-principles calculations, while formation energies are evaluated by averaging over the reference binaries (CaB₃, YB₃, and MgB₃) according to site fractions. Magnetic exchange interactions (J_{ij}^m) for the stoichiometric compounds are computed using the Liechtenstein linear-response formalism, and temperature-dependent magnetic properties are obtained through Monte Carlo simulations. This multiscale framework enables us to elucidate the fundamental coupling among magnetism, alloy stability, and hydrogen storage performance. In particular, we reveal that strong ferromagnetism in Co-based alloys destabilizes the AB₃ phase, while Ni substitution suppresses magnetism and restores thermodynamic stability, thereby resolving the intrinsic magnetism–stability trade-off that constrains optimization of hydrogen storage alloys.

Methods

The crystal structures of stoichiometric AB₃ compounds (A = Ca, Y, Mg; B = Co, Ni) with rhombohedral space group $R\bar{3}m$ (No. 166), as illustrated in **Figure 1**, were fully

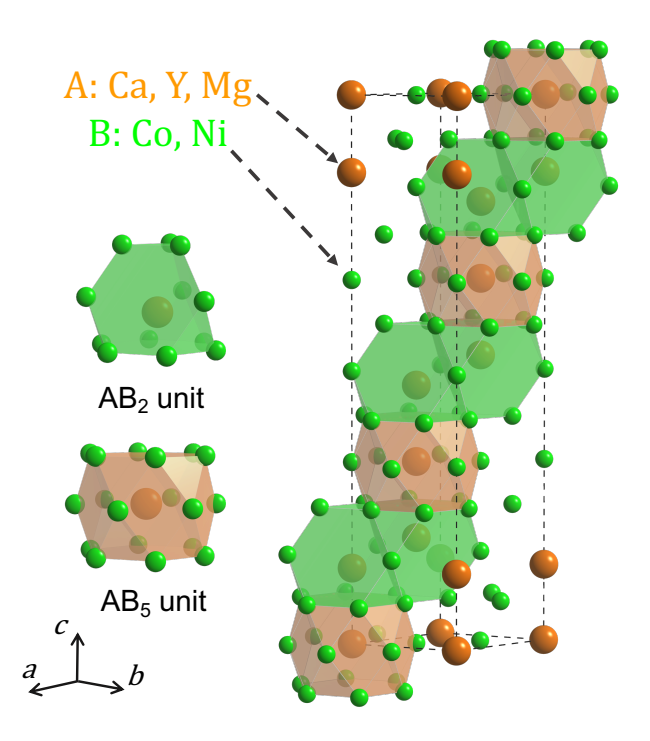


Figure 1: Crystal structure of stoichiometric AB_3 compounds (A = Ca, Y, Mg; B = Co, Ni) with rhombohedral space group $R\bar{3}m$ (No. 166). The structure can be conceptualized as a combination of AB_2 structural units (highlighted in orange) and AB_5 structural units (highlighted in green), representing two-thirds and one-third contributions, respectively. Large orange spheres represent A-site atoms (Ca, Y, or Mg) occupying both 3a (AB_5 unit) and 6c (AB_2 unit) Wyckoff positions, while smaller green spheres represent B-site atoms (Co or Ni).

optimized using the Vienna Ab-initio Simulation Package (VASP). $^{21-23}$ The exchange—correlation functional was treated within the generalized gradient approximation (GGA) using the Perdew-Burke-Ernzerhof (PBE) functional. 24 Structural optimizations employed a Monkhorst–Pack k-point mesh of $6 \times 6 \times 3$ for the rhombohedral unit cell and a plane-wave cutoff energy of 500 eV. Both lattice parameters and atomic positions were fully relaxed until residual forces on all atoms were less than 0.001 eV/Å and the energy convergence criterion was set to 10^{-6} eV. The formation energies of these stoichiometric AB₃ compounds were calculated using VASP and subsequently used to rescale the alloy formation energies obtained from CPA calculations (see **Supporting Information** for detailed lattice parameters and formation energy values).

The electronic structure and magnetic properties of $Ca_xY_yMg_{1-x-y}Co_3$ and $Ca_xY_yMg_{1-x-y}Ni_3$ alloys were investigated using the coherent potential approximation

(CPA) as implemented in the SPR-KKR (Spin-Polarized Relativistic Korringa-Kohn-Rostoker) code. ^{25,26} The CPA method enables efficient treatment of chemical disorder by replacing the random alloy with an effective medium, making it computationally tractable to explore the entire compositional space.

For the CPA calculations, three reference crystal structures of the stoichiometric compounds ACo_3 and ANi_3 (A = Ca, Y, Mg) were employed to compute alloy total energies across different local environments. The alloy formation energy was calculated as:

$$\Delta E_{\text{form}}^{\text{Ca}_{x} Y_{y} \text{Mg}_{1-x-y} \text{B}_{3}} = \frac{1}{4} \Big[E \Big(\text{Ca}_{x} Y_{y} \text{Mg}_{1-x-y} \text{B}_{3} \Big) - x E(\text{Ca}) - y E(\text{Y}) - (1 - x - y) E(\text{Mg}) - 3 E(\text{B}) \Big], \quad (1)$$

where $E(Ca_xY_yMg_{1-x-y}B_3)$ is the total energy of the alloy per formula unit, and E(Ca), E(Y), E(Mg), and E(B) (B = Co, Ni) are the total energies per atom of the elemental constituents in their ground-state crystal structures.

Since CPA calculations are performed at fixed lattice parameters and cannot account for structural relaxation effects, we developed an averaging scheme to incorporate volume and local environment effects. Given the significant size differences among Ca, Y, and Mg atomic radii, these structural effects are expected to be substantial. The alloy formation energy was averaged over the three reference AB₃ structures according to the site fractions on the A sublattice:

$$\Delta E_{\text{form}}^{\text{Ca}_x Y_y \text{Mg}_{1-x-y} \text{B}_3}(\text{average}) = x \times \Delta E_{\text{form}}^{\text{Ca}_x Y_y \text{Mg}_{1-x-y} \text{B}_3}(\text{CaB}_3 \text{ structure})$$

$$+ y \times \Delta E_{\text{form}}^{\text{Ca}_x Y_y \text{Mg}_{1-x-y} \text{B}_3}(\text{YB}_3 \text{ structure})$$

$$+ (1 - x - y) \times \Delta E_{\text{form}}^{\text{Ca}_x Y_y \text{Mg}_{1-x-y} \text{B}_3}(\text{MgB}_3 \text{ structure}).$$
(2)

This weighted averaging scheme reflects the contributions of Ca, Y, and Mg to the alloy energetics based on their relative occupancies on the A site, providing a first-order approximation to account for volume and local structural effects that are not captured by the rigid-lattice CPA approach.

The theoretical limit of gravimetric hydrogen density (wt%) of the metal hydride $Ca_xY_yMg_{1-x-y}B_3H_7$ (B = Co, Ni) is calculated using the molecular weight ratio of hydrogen to the total compound mass: ¹⁵

wt% of H₂ =
$$\frac{7 M_{\text{H}}}{x M_{\text{Ca}} + y M_{\text{Y}} + (1 - x - y) M_{\text{Mg}} + 3 M_{\text{B}} + 7 M_{\text{H}}} \times 100\%$$
 (3)

Magnetic exchange coupling constants (J_{ij}^m) for stoichiometric AB₃ alloys were calculated using the Liechtenstein formula within linear response theory as implemented in SPR-KKR. ²⁷ This approach provides a first-principles determination of the magnetic interactions by evaluating the response of the electronic system to small perturbations in the local magnetic moments. The corresponding classical Heisenberg Hamiltonian, including the effect of an external magnetic field, is expressed as: ^{28,29}

$$H_{\text{magnetic}} = -\sum_{\langle ij\rangle} J_{ij}^{m} \overrightarrow{S}_{i} \cdot \overrightarrow{S}_{j} - g\mu_{\text{B}} \sum_{i} \overrightarrow{H}_{\text{ext}} \cdot \overrightarrow{S}_{i}, \tag{4}$$

where the first term describes the exchange interactions between normalized spins \overrightarrow{S}_i and \overrightarrow{S}_j , with $J^m_{ij} > 0$ favoring ferromagnetic (parallel) alignment and $J^m_{ij} < 0$ favoring antiferromagnetic (antiparallel) alignment. The second term represents the Zeeman interaction with an external magnetic field $\overrightarrow{H}_{\rm ext}$.

Temperature-dependent magnetic properties, including magnetization and magnetic phase transitions, were investigated using Monte Carlo simulations based on the Metropolis algorithm. The simulations employed a $16 \times 16 \times 8$ supercell containing 73,728 spins with periodic boundary conditions. Each Monte Carlo run consisted of 200,000 steps, with the first 100,000 steps discarded for thermalization to ensure equi-

librium sampling. Magnetic susceptibility was calculated as the derivative of magnetization with respect to temperature, and Curie temperatures were determined from the peak positions in the susceptibility curves.

Results and Discussion

ACo₃ Systems: Strong Magnetism Limits Stability

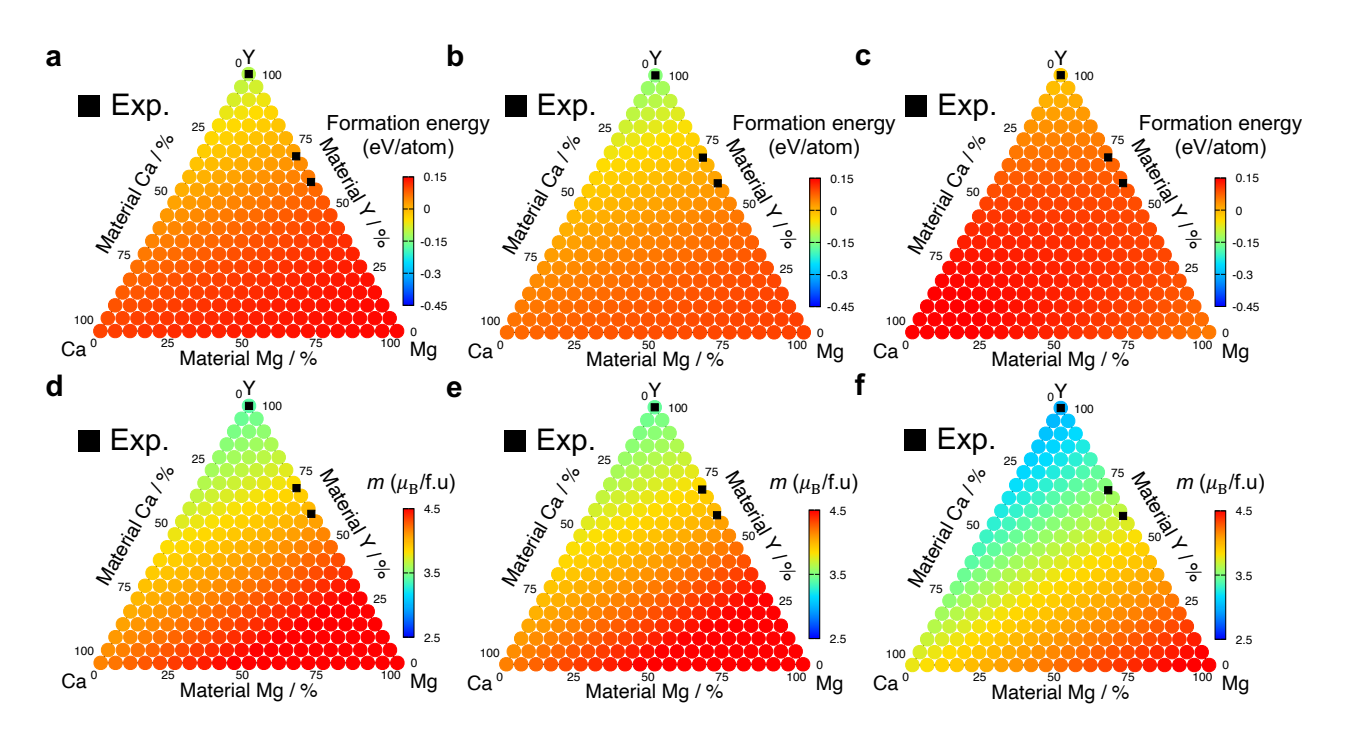


Figure 2: Formation energy diagrams of $Ca_xY_yMg_{1-x-y}Co_3$ calculated using Eq. 1 with the crystal structures of $CaCo_3$ (a), YCo_3 (b), and $MgCo_3$ (c). Corresponding total magnetic moment diagrams of $Ca_xY_yMg_{1-x-y}Co_3$ with the crystal structures of $CaCo_3$ (d), YCo_3 (e), and $MgCo_3$ (f). Formation energies are given in eV per formula unit, and magnetic moments in μ_B per formula unit. Black squares indicate compounds reported in previous experimental studies. ^{14,15}

The formation energy diagrams of $Ca_xY_yMg_{1-x-y}Co_3$ alloys, calculated using the lattice parameters of $CaCo_3$, YCo_3 , and $MgCo_3$ as references, are shown in **Figure 2(a-c)**. Black squares indicate experimentally reported compositions. ^{14,15} Formation energies were evaluated using Eq. 1 and subsequently averaged according to Eq. 2. Two primary factors govern the energy landscape: elemental composition and structural

reference lattice. For each stoichiometric compound (CaCo₃, YCo₃, MgCo₃), the lowest formation energy occurs when adopting its own optimized lattice. Using CaCo₃ or YCo₃ lattice parameters, the minimum energies are found at the Y-rich corner, defining a thermodynamically stable triangular region (green to orange coloring) with negative formation energies. Within these structural frameworks, Ca-rich compositions show slightly higher energies, while Mg-rich compositions exhibit the largest values, indicating reduced stability. In contrast, when the MgCo₃ lattice is used as the reference, formation energies increase across most of the compositional range, with only the immediate Mg-rich region maintaining relatively low values. Nonetheless, the Y-rich corner still provides the most favorable energetics. This trend originates from the significantly smaller unit cell volume of MgCo₃ compared to CaCo₃ and YCo₃, which induces a strain effect when larger Ca or Y atoms are substituted (see **Supporting Information** for detailed lattice parameter comparisons).

The corresponding total magnetic moment diagrams are presented in Figure 2(d-f). A clear correlation emerges: the lowest total magnetic moments consistently occur at the Y-rich corner, whereas increasing Ca or Mg content enhances the magnetic moment. This trend parallels the formation energy distributions for the CaCo₃ and YCo₃ lattices, where the stable triangular Y-rich region corresponds to intermediate magnetic moments (green to yellow coloring). In contrast, the MgCo₃ lattice exhibits more complex magnetic behavior due to volume constraints, showing suppressed magnetization near the Y- and Ca-rich regions but overall larger variation in total magnetic moments.

The compositionally averaged formation energy and total magnetic moment diagrams of $Ca_xY_yMg_{1-x-y}Co_3$, obtained by weighted averaging over the three reference structures using Eq. 2, are shown in **Figure 3(a, b)**. The corresponding theoretical gravimetric hydrogen density of $Ca_xY_yMg_{1-x-y}Co_3H_7$ from Eq. 3 is presented in **Figure 3(c)**. The averaged formation energy diagram reveals a stable triangular region concentrated near the Y-rich corner, where negative formation energies confirm thermodynamic feasibility. Within this region, Ca substitution is more favorable than Mg replacement, as the maximum Ca content for stability exceeds that of Mg. The color

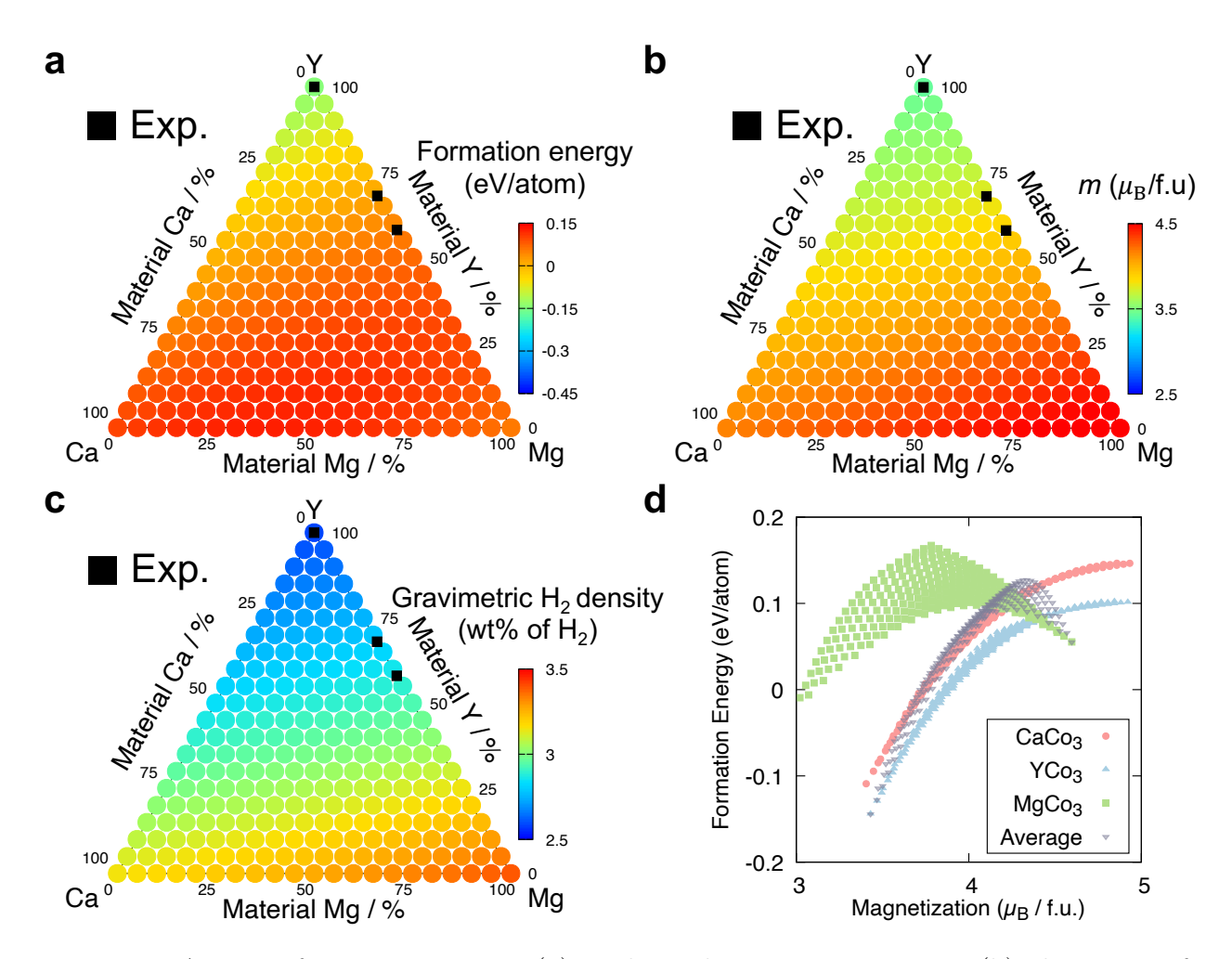


Figure 3: Average formation energy (a) and total magnetic moment (b) diagrams of $Ca_xY_yMg_{1-x-y}Co_3$ calculated using Eq. 2. (c) Theoretical gravimetric hydrogen density diagram of $Ca_xY_yMg_{1-x-y}Co_3H_7$ assuming complete hydrogenation from Eq. 3. Formation energies are given in eV per formula unit, magnetic moments in μ_B per formula unit, and hydrogen densities in weight percent. Black squares indicate compounds reported in previous experimental studies. ^{14,15} (d) Formation energy versus total magnetic moment of $Ca_xY_yMg_{1-x-y}Co_3$ with $CaCo_3$ (light-red), YCo₃ (light-blue), and MgCo₃ (light-green) structures. The average formation energy versus average total magnetic moment (black) is estimated by using Eq. 2.

gradient from green to orange delineates this stability window, emphasizing that sufficient Y incorporation is essential for structural stability. This stability requirement, however, directly conflicts with hydrogen storage optimization. The gravimetric density map shows that higher Ca and Mg concentrations enhance hydrogen capacity due to their lower atomic masses relative to Y. Compositions at the Mg-rich corner reach the highest theoretical density ($\sim 3.39 \text{ wt}\%$), but these states possess positive formation

energies and are thus unstable. The experimentally realized $Y_{0.68}Mg_{0.32}Co_3$ composition reported by Sato et al. lies precisely at the edge of the stable triangular region, achieving a gravimetric density of ~ 2.80 wt%. This composition delivers performance comparable to the best $Y_xCa_{1-x}Co_3$ alloys, yet highlights the intrinsic limitation of Co-based systems: further improvement is fundamentally constrained by the stability-capacity trade-off. Importantly, the stability map mirrors the magnetic moment distribution. The lowest total magnetic moments appear in the Y-rich corner and correlate with negative formation energies, whereas increasing Ca or Mg content enhances magnetization and destabilizes the lattice. These results establish that strong ferromagnetism is inherently detrimental to structural stability in Co-based AB₃ alloys.

The formation energy as a function of total magnetic $Ca_xY_yMg_{1-x-y}Co_3$ alloys, evaluated using three reference structures and the averaged values from Eq. 2, is shown in **Figure 3(d)**. In the $CaCo_3$ and YCo_3 structures, which possess relatively large unit-cell volumes, a clear one-to-one correlation between total magnetic moment and formation energy is observed: the formation energy systematically increases with increasing magnetization. This monotonic behavior indicates that magnetism is the dominant factor governing alloy stability under these structural conditions. In contrast, the MgCo₃ structure, with its much smaller equilibrium volume, exhibits no such one-to-one correspondence-compositions with similar total magnetic moments show distinct formation energies. This breakdown of the correlation suggests that in the compact MgCo₃ lattice, magnetism couples more strongly with lattice volume and electronic degrees of freedom as the strain effect, thereby weakening the direct magnetism-stability dependence. magnetization ternary diagrams in Figure 2(d-f), compositions with low total magnetic moments (left-hand side) correspond to Y-rich regions near YCo₃, whereas those with high magnetic moments (right-hand side) correspond to Mg-rich regions near MgCo₃. Among the three end-member compounds, each structure attains its lowest formation energy when evaluated using its own lattice parameters. The average formation energy versus average total magnetic moment derived from Eq. 2 smoothly approaches the corresponding stoichiometric structures as the A-site composition approaches their respective limits: starting from YCo₃ with the lowest formation energy, crossing the CaCo₃ structure, and finally reaching MgCo₃ with the highest magnetization.

Table 1: Magnetic moments of stoichiometric ACo₃ compounds (A = Ca, Y, Mg) from SPR-KKR calculations.

Materials	$m_{ m total}$	$m_{\mathrm{A}(3a)}$	$m_{\rm A(6c)}$	$m_{\mathrm{Co}(3b)}$	$m_{\text{Co}(6c)}$	$m_{\mathrm{Co}(18h)}$
ACo_3	$\mu_{ m B}/{ m f.u.}$	$(\mu_{ m B}/{ m atom})$				
CaCo ₃	4.155	-0.254	-0.320	1.532	1.637	1.426
YCo_3	3.430	-0.311	-0.375	1.197	1.392	1.229
$MgCo_3$	4.597	-0.124	-0.184	1.555	1.639	1.575

To clarify the relationship between magnetism and stability, we analyze the electronic structures of stoichiometric CaCo₃, YCo₃, and MgCo₃. Figure 4(a–c) shows the total and partial densities of states (DOS). In all cases, the Co d states dominate near the Fermi level, while the contributions from Ca, Y, and Mg are comparatively small. Magnetic moment analysis (Table 1) confirms that Co atoms carry the primary magnetic moments, whereas the A-site atoms (Ca, Y, Mg) contribute only small antiparallel moments, producing a ferrimagnetic configuration. A key distinction emerges in YCo₃, which exhibits a markedly reduced total magnetic moment (3.430 μ_B /f.u.) compared with CaCo₃ (4.155 μ_B /f.u.) and MgCo₃ (4.597 μ_B /f.u.). This reduction originates from Co atoms adopting a low-spin state due to weaker exchange splitting, combined with the larger antiferromagnetic contribution from Y.

The magnetic exchange coupling constants in **Figure 4(d-f)** provide further insights. A–A interactions are negligible, while Co–Co couplings are strongly positive, confirming robust ferromagnetic interactions. A–Co couplings are weak and negative, consistent with the ferrimagnetic arrangement. Importantly, the Co–Co exchange couplings in YCo₃ are substantially weaker, reflecting its low-spin Co state. Consequently, the mean-field Curie temperature is significantly reduced to 754.6 K, compared with 1042.7 K for CaCo₃ and 1167.3 K for MgCo₃. These results demonstrate that Y sub-

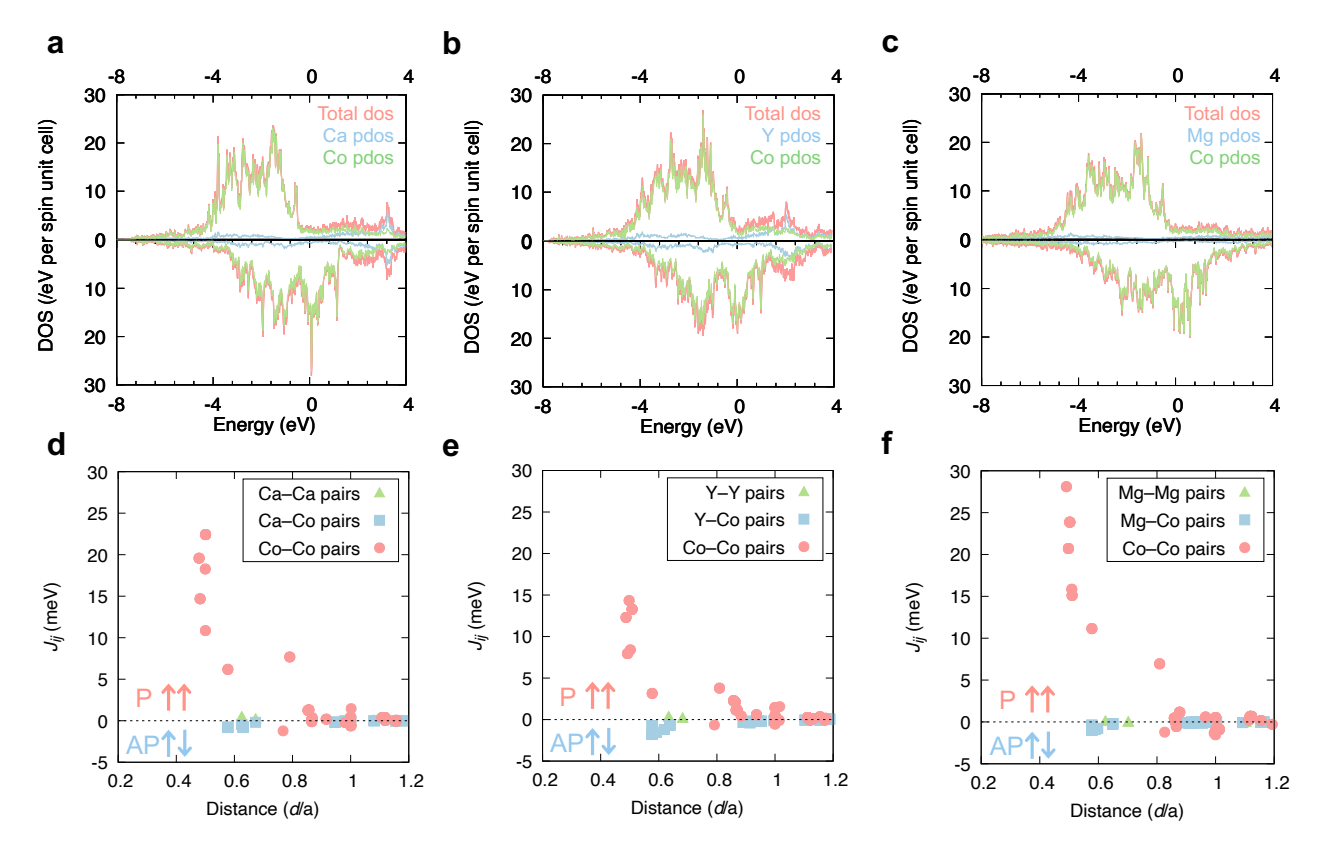


Figure 4: Total and partial density of states (DOS) of $CaCo_3$ (a), YCo_3 (b), and $MgCo_3$ (c). The total DOS is shown as light-red curves, while the partial DOS of A atoms (Ca, Y, Mg) and Co atoms are shown as light-blue and light-green curves, respectively. The partial DOS corresponds to the sum over all atoms of the same type in the unit cell. Magnetic exchange coupling constants of $CaCo_3$ (d), YCo_3 (e), and $MgCo_3$ (f), where A–A, A–Co, and Co–Co pairs are denoted by light-green triangles, light-blue squares, and light-red circles, respectively. Spin tends to parallel (P) in the case of $J_{ij} > 0$, while $J_{ij} < 0$ favors antiparallel (AP).

stitution stabilizes the Co-based system by suppressing magnetic exchange through low-spin Co states, directly linking reduced magnetism to enhanced structural stability.

Monte Carlo simulations yield more realistic estimates of the magnetic transition temperatures. As shown in **Figure 5(a)**, the temperature dependence of magnetization and susceptibility for CaCo₃, YCo₃, and MgCo₃ clearly reveals ferromagnetic-to-paramagnetic transitions, with Curie temperatures identified from the susceptibility maxima: 602 K (CaCo₃), 474 K (YCo₃), and 697 K (MgCo₃). These values, while lower than the mean-field estimates, preserve the same trend of suppressed ordering

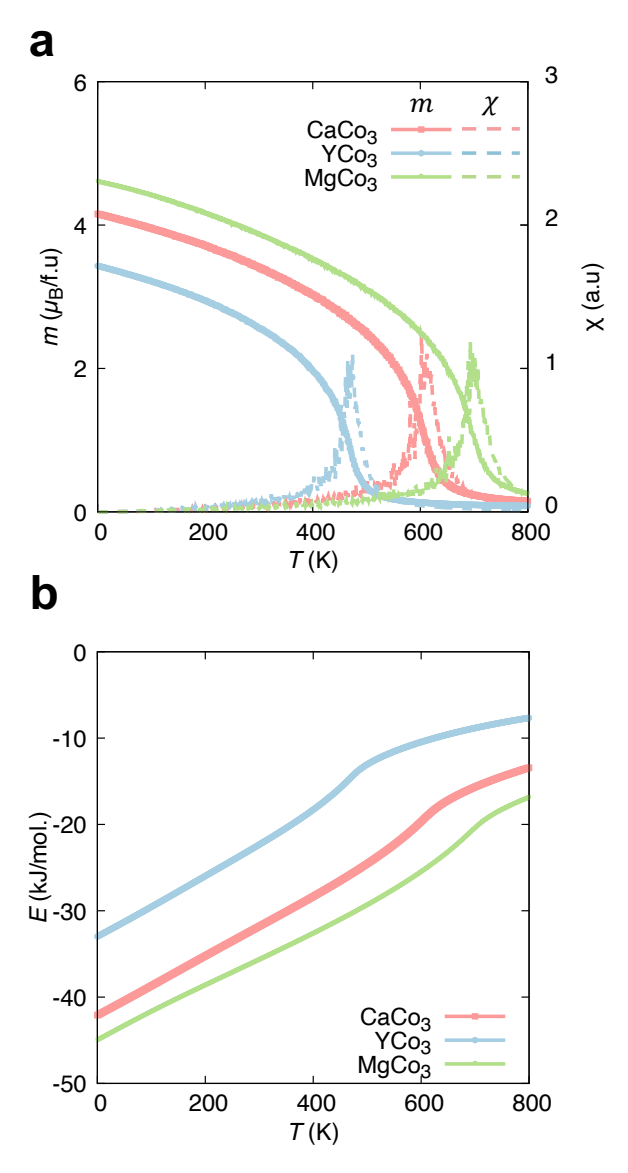


Figure 5: Temperature dependence of (a) magnetization and magnetic susceptibility, and (b) magnetic energy for CaCo₃, YCo₃, and MgCo₃. Magnetization and magnetic energy are shown as solid curves in light-red, light-blue, and light-green for CaCo₃, YCo₃, and MgCo₃, respectively. Magnetic susceptibility is shown as dashed curves with the same color scheme.

temperature in YCo₃. The magnetic energy profiles in **Figure 5(b)** further highlight this behavior. All compounds exhibit large negative magnetic energies at 0 K, with MgCo₃ showing the most negative value, consistent with its highest saturation magnetization. The steepest energy variations occur at the Curie temperatures, reflecting the peak in magnetic heat capacity. Together, these results demonstrate that strong ferromagnetism, manifested in high magnetic moments and elevated Curie temperatures,

correlates with reduced thermodynamic stability in Co-based AB₃ alloys. Notably, Mg incorporation, while favorable for achieving high hydrogen storage density, amplifies ferromagnetic interactions and thereby destabilizes the lattice. This intrinsic trade-off underscores the need to explore alternative B-site elements with weaker magnetic interactions to balance hydrogen storage capacity and structural stability.

ANi₃ Systems: Reduced Magnetism Enables Enhanced Stability

Table 2: Magnetic moments of stoichiometric ANi₃ (A = Ca, Y, Mg) from SPR-KKR.

Materials	$m_{ m total}$	$m_{\mathrm{A}(3a)}$	$m_{\mathrm{A}(6c)}$	$m_{\mathrm{Ni}(3b)}$	$m_{ m Ni(6c)}$	$m_{\mathrm{Ni}(18h)}$
ANi_3	$(\mu_{ m B}/{ m f.u.})$	$(\mu_{ m B}/{ m atom})$				
CaNi ₃	0.768	-0.058	-0.070	0.165	0.324	0.281
YNi_3	0.000	0.000	0.000	0.000	0.000	0.000
$MgNi_3$	0.793	-0.023	-0.033	0.198	0.312	0.274

The electronic structures of CaNi₃, YNi₃, and MgNi₃, shown in Figure 6(a-c), reveal fundamentally different magnetic behavior compared to their Co-based counterparts, reshaping the stability landscape for hydrogen storage applications. Ni d states dominate near the Fermi level, as in Co systems, but the exchange splitting is substantially weaker due to the nearly filled d^9 configuration of Ni, in contrast to the d^7 configuration of Co. Magnetic moment analysis (Table 2) highlights this transformation: CaNi₃ and MgNi₃ exhibit very small total moments of 0.768 and 0.793 $\mu_{\rm B}/{\rm f.u.}$, respectively—over five times smaller than their Co analogues (4.155 and 4.597 $\mu_{\rm B}/{\rm f.u.}$). Most notably, YNi₃ is fully nonmagnetic, with zero moments on all atomic sites, in stark contrast to YCo₃ (3.430 $\mu_{\rm B}/{\rm f.u.}$). This suppression arises from Ni approaching a filled d^{10} configuration, where crystal field effects favor a low-spin or nonmagnetic state. In weakly magnetic CaNi₃ and MgNi₃, Ni atoms at different crystallographic positions (3b, 6c, 18b) display small but varying moments (0.165–0.324 $\mu_{\rm B}/{\rm atom}$), reflecting local environment differences within the rhombohedral structure. A-site atoms

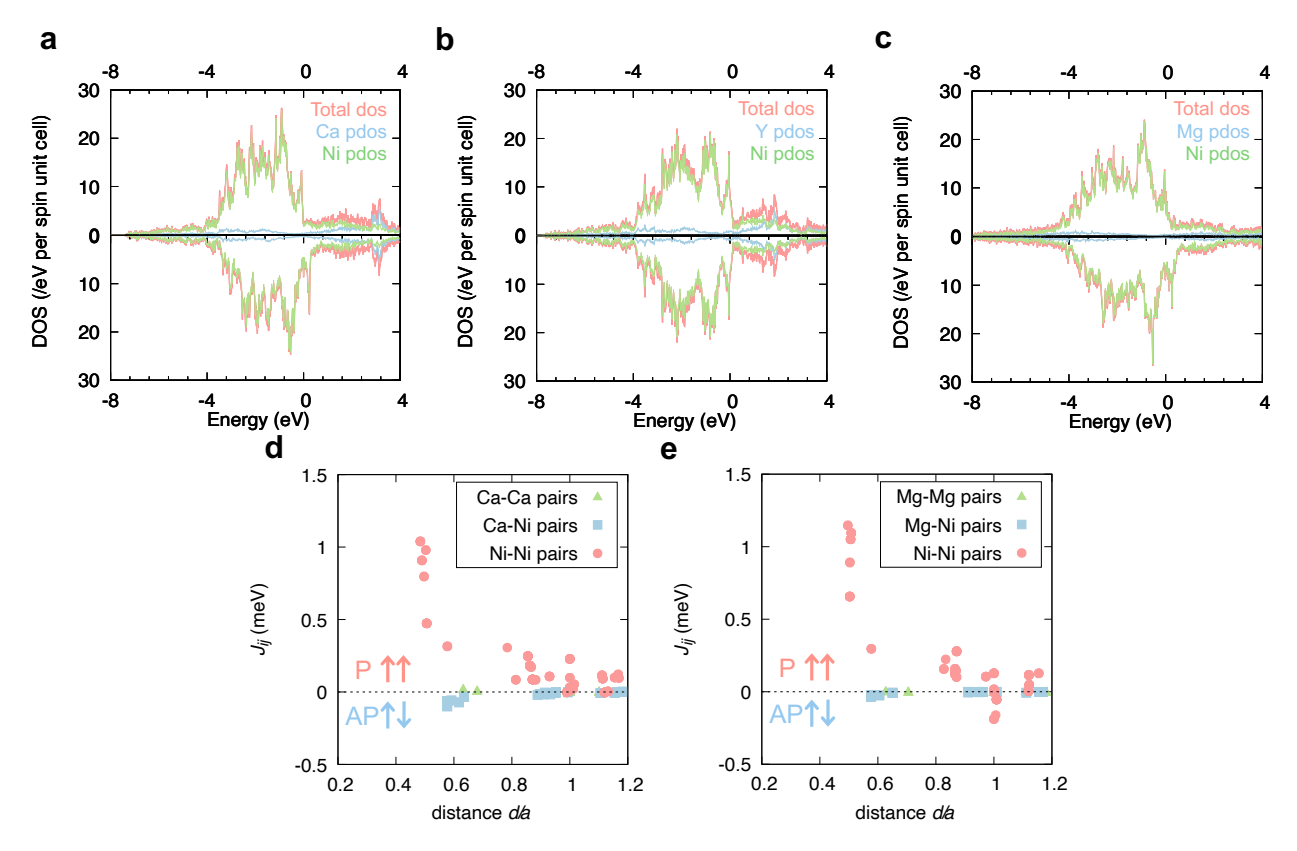


Figure 6: Total and partial density of states (DOS) of $CaNi_3$ (a), YNi_3 (b), and $MgNi_3$ (c). The total DOS is shown as light-red curves, while the partial DOS of A atoms (Ca, Y, Mg) and Ni atoms are shown as light-blue and light-green curves, respectively. The partial DOS corresponds to the sum over all atoms of the same type in the unit cell. Magnetic exchange coupling constants of $CaNi_3$ (d) and $MgNi_3$ (e), where A–A, A–Ni, and Ni–Ni pairs are denoted by light-green triangles, light-blue squares, and light-red circles, respectively. Spin tends to parallel (P) in the case of $J_{ij} > 0$, while $J_{ij} < 0$ favors antiparallel (AP).

contribute minor antiparallel moments, as in the Co systems, but with greatly reduced magnitude. The ferrimagnetic configuration is preserved, yet the overall magnetization is substantially suppressed. This dramatic reduction in magnetic interactions directly relaxes stability constraints, providing a broader compositional space for designing thermodynamically robust, high-capacity Ni-based AB₃ hydrogen storage alloys.

The magnetic exchange coupling constants for CaNi₃ and MgNi₃, shown in **Figure 6(d, e)**, are substantially weaker than those in Co-based systems. Ni–Ni interactions, while remaining ferromagnetic, are an order of magnitude smaller than the corresponding Co–Co couplings, directly reflecting the reduced magnetic moments on

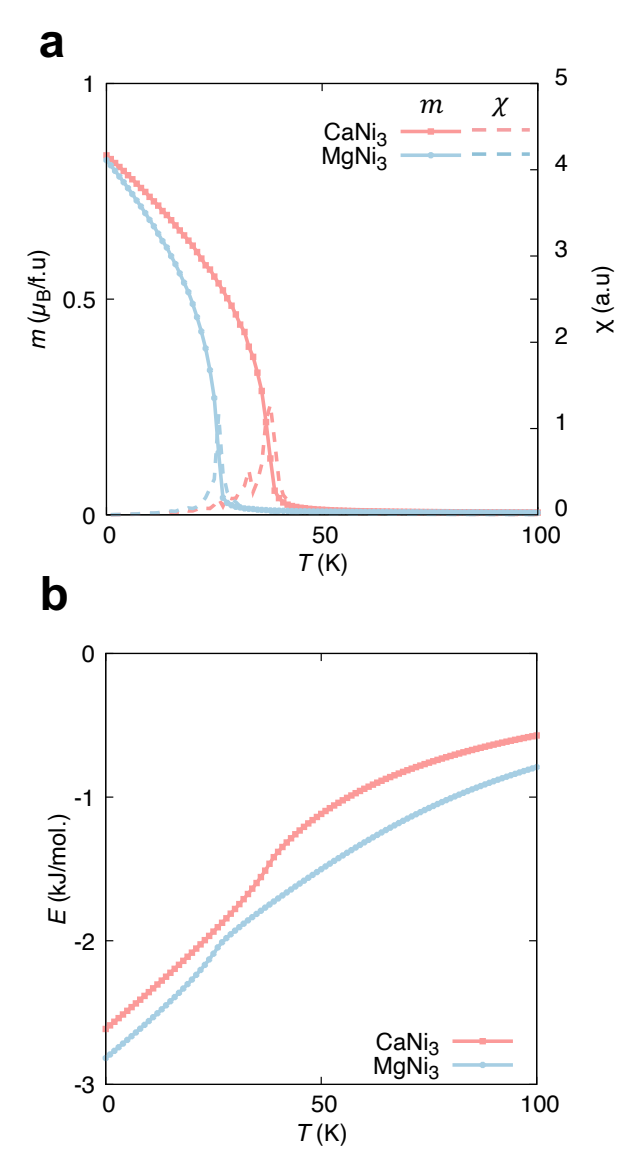


Figure 7: Temperature dependence of (a) magnetization and magnetic susceptibility, and (b) magnetic energy for CaNi₃ and MgNi₃. Magnetization and magnetic energy are shown as solid curves in light-red and light-blue for CaNi₃ and MgNi₃, respectively. Magnetic susceptibility is shown as dashed curves with the same color scheme.

Ni sites and explaining the dramatically lower magnetic transition temperatures. A–Ni interactions remain weakly antiferromagnetic, consistent with the ferrimagnetic ground state, but their contribution to the overall magnetic behavior is minimal due to the weak Ni magnetism. Temperature-dependent magnetic properties, presented in **Figure 7**, further confirm this behavior. Mean-field estimates yield Curie temperatures of 88.6 K (CaNi₃) and 66.6 K (MgNi₃), substantially lower than Co analogues (1042.7)

K and 1167.3 K, respectively). Monte Carlo simulations predict even lower transition temperatures of 38 K and 26 K, indicating that both compounds exhibit only weak ferromagnetism at very low temperatures and are effectively paramagnetic under typical hydrogen storage conditions. The magnetic energy evolution (Figure 7(b)) shows much smaller negative values at 0 K compared to Co-based systems, with steepest gradients near the Curie temperatures, reflecting the low magnetic stabilization energy. These results demonstrate that magnetic interactions in Ni-based AB₃ alloys play a minimal role in the total energy balance, fundamentally altering thermodynamic stability relative to strongly magnetic Co-based systems. Replacing Co with Ni transforms the electronic and magnetic landscape, removing the primary destabilizing factor in Co alloys and enabling access to previously inaccessible compositional regions. This reduction in magnetic interactions allows the design of thermodynamically stable alloys while preserving the structural framework necessary for high-capacity hydrogen storage.

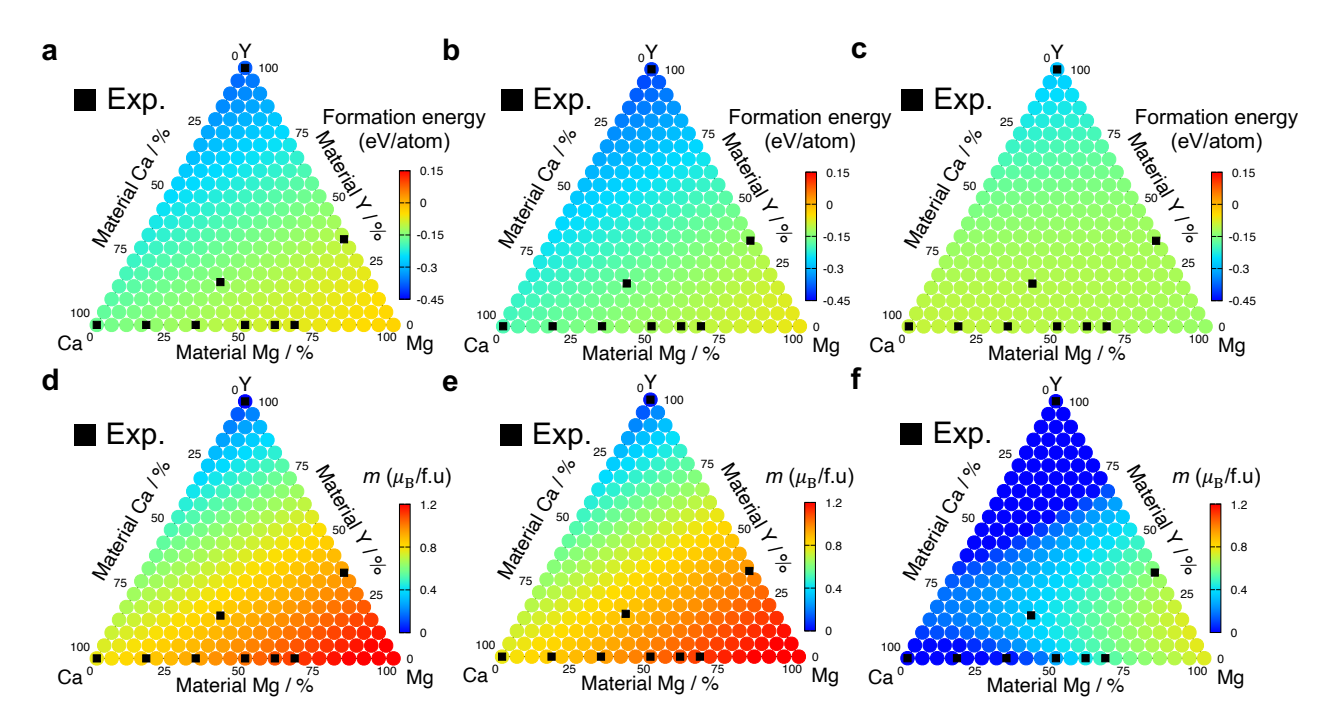


Figure 8: Formation energy diagrams of $Ca_xY_yMg_{1-x-y}Ni_3$ calculated using Eq. 1 with the crystal structures of $CaNi_3$ (a), YNi_3 (b), and $MgNi_3$ (c). Corresponding total magnetic moment diagrams of $Ca_xY_yMg_{1-x-y}Ni_3$ with the crystal structures of $CaNi_3$ (d), YNi_3 (e), and $MgNi_3$ (f). Compounds reported in previous experimental studies are indicated by black squares. $^{11,16-20}$

The formation energy diagrams of $Ca_xY_yMg_{1-x-y}Ni_3$ alloys, calculated using the three reference structures, are shown in Figure 8(a–c). Compared to Co-based systems, a remarkable transformation is observed: all compositions across the ternary diagram exhibit negative formation energies, indicating universal thermodynamic stability. While the Y-rich corner remains the most stable region, the energy differences across the compositional space are substantially reduced, reflecting a more uniform stability landscape. The total magnetic moment diagrams in Figure 8(d–f) further illustrate this trend. YNi₃ retains zero magnetization across all reference structures, whereas compositions with increasing Ca and Mg content develop only weak ferromagnetism. Crucially, the magnetic moments remain far smaller than those in Co-based alloys, consistent with the enhanced thermodynamic stability. This analysis demonstrates that the suppression of magnetic interactions in Ni-based AB₃ alloys fundamentally alleviates the magnetism-driven stability constraints observed in Co systems, opening broad compositional space for stable, high-capacity hydrogen storage materials.

The averaged formation energy and total magnetic moment diagrams for $Ca_xY_yMg_{1-x-y}Ni_3$ are presented in Figure 9(a, b), with the corresponding theoretical gravimetric hydrogen densities from Eq. 3 shown in Figure 9(c). The universally negative formation energies mark a significant improvement over Co-based systems, as compositions with high hydrogen storage potential are now thermodynamically accessible. The hydrogen density distribution closely mirrors that of the Co system, with maximum values near the Mg-rich corner reaching ~ 3.40 wt% for pure MgNi₃H₇. Importantly, the experimentally known composition $CaMg_2Ni_9$ ($Ca_{0.33}Mg_{0.67}Ni_3$) achieves both high hydrogen storage density (~ 3.32 wt%) and sufficient thermodynamic stability. ^{11,19} Most significantly, our calculations identify the previously unexplored Mg-rich corner of the ternary diagram as a promising compositional region that combines high theoretical hydrogen capacity with robust stability. This finding extends beyond known experimental compositions, highlighting new synthetic targets for high-performance hydrogen storage materials. The key enabling factor is the weak magnetism in Ni-based systems. Unlike Co-based alloys, where strong

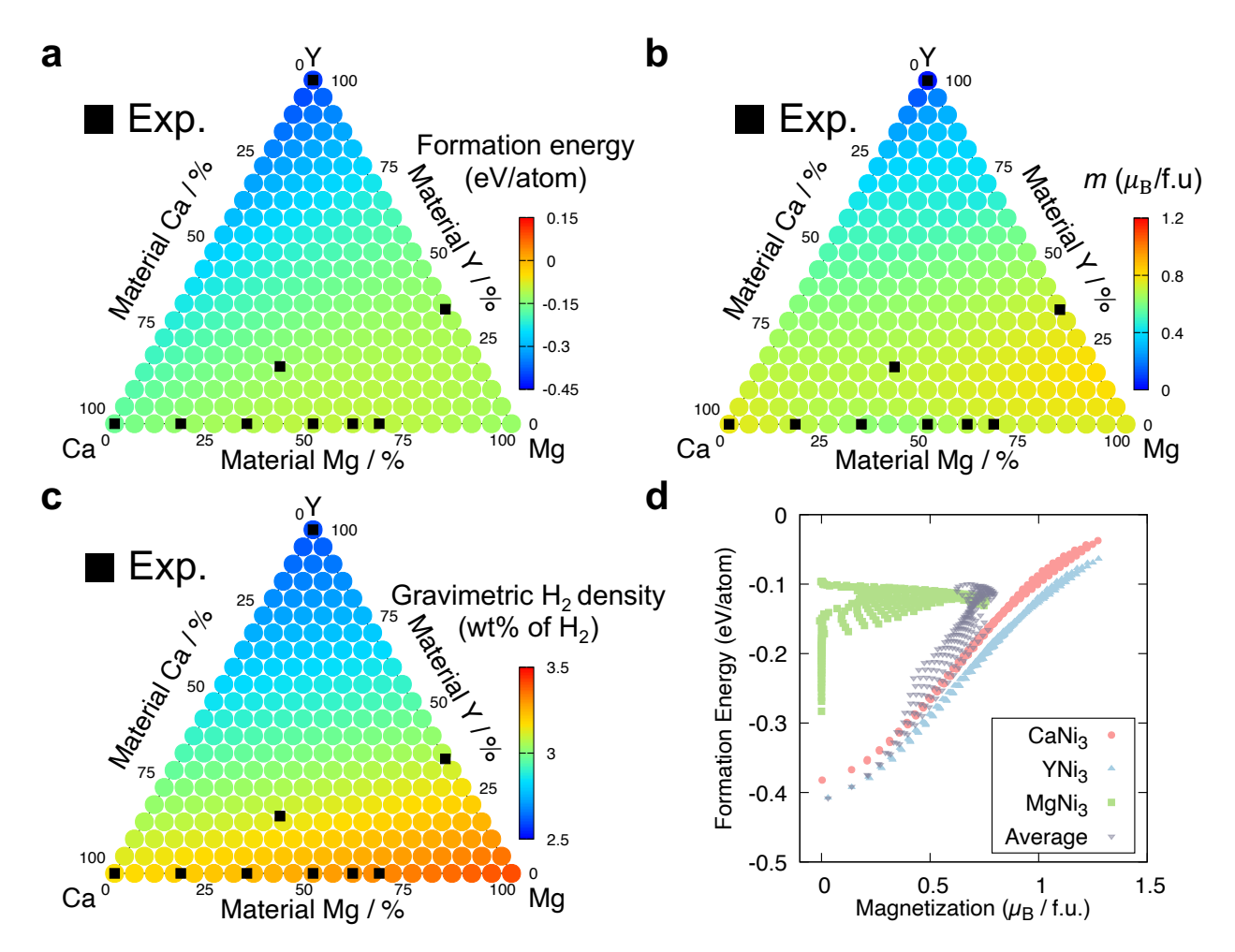


Figure 9: Average formation energy (a) and total magnetic moment (b) diagrams of $Ca_xY_yMg_{1-x-y}Ni_3$ calculated using Eq. 2. (c) Theoretical gravimetric hydrogen density of $Ca_xY_yMg_{1-x-y}Ni_3H_7$ (wt%) from Eq. 3. Formation energies are given in eV per formula unit and magnetic moments in μ_B per formula unit. Black squares indicate compounds reported in previous experimental studies. ^{11,16–20} (d) Formation energy versus total magnetic moment of $Ca_xY_yMg_{1-x-y}Ni_3$ with $CaNi_3$ (light-red), YNi_3 (light-blue), and $MgNi_3$ (light-green) structures. The average formation energy versus average total magnetic moment (black) is estimated by using Eq. 2.

ferromagnetism imposes a fundamental stability barrier for high-capacity compositions, Ni-based AB₃ alloys maintain thermodynamic stability across the entire compositional range while preserving comparable hydrogen storage densities. This demonstrates that suppression of magnetic interactions is critical for reconciling high hydrogen capacity with structural stability in AB₃-type hydrides.

The formation energy as a function of total magnetic moment for $Ca_xY_yMg_{1-x-y}Ni_3$

alloys, evaluated using three reference structures and the averaged values from Eq. 2, is shown in Figure 9(d). Unlike the Co-based alloys, the Ni-based alloys system exhibits considerably lower magnetic moments, ranging from zero to approximately $1.5~\mu_{\rm B}/{\rm f.u.}$, reflecting the weaker ferromagnetic character of Ni compared to Co. The reference structures CaNi₃ and YNi₃ display a similar trend to CaCo₃ and YCo₃, where the formation energy increases with increasing magnetization. This one-to-one correlation in the CaNi₃ and YNi₃ structures suggests that the Ni-based alloys behave similarly to the Co-based alloys when evaluated with the large lattice volumes characteristic of CaNi₃ and YNi₃. On the other hand, MgNi₃, with its much smaller lattice volume, shows a complex dependence where magnetism can disappear at both the Y-rich and Ca-rich corners, while the Mg-rich region retains the highest total magnetic moment. The averaged formation energy, derived from Eq. 2, provides a smooth interpolation between the three structures, with compositions approaching YNi₃ (low magnetization) being energetically most favorable, and those near the higher-magnetization regime corresponding to Ca-enriched and Mg-enriched compositions.

Summary

Our comprehensive investigation establishes the decisive role of magnetism in governing the structural stability of AB_3 -type alloys and clarifies its impact on hydrogen storage optimization. Across the $Ca_xY_yMg_{1-x-y}Co_3$ and $Ca_xY_yMg_{1-x-y}Ni_3$ systems, formation energy is strongly correlated with total magnetic moment. In Co-based alloys with large lattice volumes, such as $CaCo_3$ and YCo_3 , the formation energy increases monotonically with magnetization, indicating that strong ferromagnetism intrinsically destabilizes the AB_3 lattice. This magnetism–stability correlation weakens in $MgCo_3$, where magnetic, electronic, and lattice degrees of freedom become strongly coupled. While Mg-rich regions in Co-based alloy offer high gravimetric densities, their stability is limited by strong magnetism, requiring Y substitution to suppress Co moments through a low-spin state—an intrinsic constraint to

hydrogen storage optimization. In contrast, Ni substitution fundamentally reshapes this landscape: YNi₃ is nonmagnetic, and CaNi₃ and MgNi₃ exhibit only weak spin polarization, leading to thermodynamic stability across a wide composition range. The experimentally reported CaMg₂Ni₉ exemplifies this magnetic suppression strategy, combining high capacity (~ 3.32 wt%) with good reversibility, while the Mg-rich Ni-based region identified in this work unites negative formation energies with the highest theoretical densities (up to ~ 3.40 wt%). Overall, these results establish magnetism as a key thermodynamic parameter and provide quantitative design principles for stabilizing high-capacity AB₃-type hydrogen storage materials through magnetic control. We also note that, this interesting phenomenon not only provides new design guidelines for hydrogen storage materials, but also for other types of materials and chemical reactions where AB₃-type alloys can play an essential role (e.g., batteries and catalysis).

Author contributions

H. B. Tran: Investigation, Writing - Original Draft. T. Sato: Writing - Review & Editing. R. Sato: Writing - Review & Editing. H. Saitoh: Writing - Review & Editing. S. Orimo: Funding acquisition, Supervision, Writing - Review & Editing. H. Li: Supervision, Resources, Writing - Review & Editing.

Conflicts of interest

There are no conflicts to declare.

Acknowledgements

This work was supported by The Green Technologies of Excellence (GteX) Program, Japan (Grant No. JPMJGX23H1).

Data availability

The data that support the findings of this study are available from the corresponding author upon reasonable request. Besides, the key data have also been uploaded to Digital Hydrogen Platform (DigHyd: www.dighyd.org).

References

- (1) Staffell, I.; Scamman, D.; Abad, A. V.; Balcombe, P.; Dodds, P. E.; Ekins, P.; Shah, N.; Ward, K. R. The role of hydrogen and fuel cells in the global energy system. *Energy Environ. Sci.* 2019, 12, 463–491. https://doi.org/10.1039/C8EE01157E.
- (2) Boretti, A.; Pollet, B. G. Hydrogen economy: Paving the path to a sustainable, low-carbon future. *Int. J. Hydrog. Energy*, **2024**, *93*, 307–319. https://doi.org/10.1016/j.ijhydene.2024.10.350.
- (3) Mehtab, A.; Ali, S. A.; Sadiq, I.; Shaheen, S.; Khan, H.; Fazil, M.; Pandit, N. A.; Naaz, F.; Ahmad, T. Hydrogen Energy as Sustainable Energy Resource for Carbon-Neutrality Realization. ACS Sustain. Resource Manag., 2024 1, 604–620. https://doi.org/10.1021/acssusresmgt.4c00039
- (4) Oliveira, A. M.; Beswick, R. R.; Yan, Y. A green hydrogen economy for a renewable energy society. Curr. Opin. Chem. Eng., 2021, 33, 100701. https://doi.org/10.1016/j.coche.2021.100701.
- (5) Eriksson, E. L. V.; Gray, E. M. A. Optimization and integration of hybrid renewable energy hydrogen fuel cell energy systems—A critical review. Appl. Energy, 2017, 202, 348–364. https://doi.org/10.1016/j.apenergy.2017.03.132.
- (6) Allendorf, M. D.; Stavila, V.; Snider, J. L.; Witman, M.; Bowden, M. E.; Brooks, K.; Tran, B. L.; Autrey, T. Challenges to developing materials for

- the transport and storage of hydrogen. *Nat. Chem.*, **2022**, *14*, 1214–1223. https://doi.org/10.1038/s41557-022-01056-2.
- (7) Felderhoff, M.; Weidenthaler, C.; Helmoltb, R. V.; Eberleb, U. Hydrogen storage: the remaining scientific and technological challenges. *Phys. Chem. Chem. Phys.*, 2007, 9, 2643–2653. https://doi.org/10.1039/B701563C.
- (8) Deng, J.; Bae, C.; Denlinger, A.; Miller, T. Electric Vehicles Batteries: Requirements and Challenges. Joule, 2020. 4, 511–515. https://doi.org/10.1016/j.joule.2020.01.013.
- (9) Zhang, T.; Uratani, J.; Huang, Y.; Xu, L.; Griffiths, S.; Ding, Y. Hydrogen liquefaction and storage: Recent progress and perspectives. *Renew. Sust. Energ.*, 2023, 176, 113204. https://doi.org/10.1016/j.rser.2023.113204.
- (10) Yang, J.; Sudik, A.; Wolverton, C. Destabilizing LiBH₄ with a Metal (M = Mg, Al, Ti, V, Cr, or Sc) or Metal Hydride (MH₂ = MgH₂, TiH₂, or CaH₂). J. Phys. Chem. C, 2007, 111, 19134–19140. https://doi.org/10.1021/jp076434z.
- (11) Kadir, K.; Kuriyama, N.; Sakai, T.; Uehara, I.; Eriksson, L. Structural investigation and hydrogen capacity of CaMg₂Ni₉: a new phase in the AB₂C₉ system isostructural with LaMg₂Ni₉. J. Alloy. Compd., 1999, 284, 145–154. https://doi.org/10.1016/S0925-8388(98)00965-7.
- (12) Pasquini, L.; Sakaki, K.; Akiba, E. et al. Magnesium- and intermetallic alloys-based hydrides for energy storage: modelling, synthesis and properties. *Prog. Energy*, **2022**, *4*, 032007. https://doi.org/10.1088/2516-1083/ac7190.
- (13) Iwase, K.; Kimura, T.; Mori, K. Y-Co binary alloys with superlattice structures: Relationship between hydrogenation cyclic stability and crystal structures of hydride phases. *Int. J. Hydrogen Energy*, **2025**, *139*, 62–68. https://doi.org/10.1016/j.ijhydene.2025.05.258.

- (14) Liu, J.; Broom, D. P.; Georgiev, P. A. L.; Ross, D. K. Magnetic properties of the YCo₃-H system. J. Alloy. Compd., 2003, 356-357, 174-177. https://doi.org/10.1016/S0925-8388(03)00260-3
- (15) Sato, T.; Saitoh, H.; Utsumi, R.; Ito, J.; Obana, K.; Nakahira, Y.; Sheptyakov, D.; Honda, T.; Sagayama, H.; Takagi, S.; Kono, T.; Yang, H.; Luo, W.; Lombardo, L.; Züttel, A.; Orimo, S. -i. Synthesis, crystal structure, and hydrogen storage properties of an ab3-based alloy synthesized by disproportionation reactions of AB₂-based alloys. J. Phys. Chem. C, 2025, 129, 2865–2873. https://doi.org/10.1021/acs.jpcc.4c06759
- (16) Chen, J.; Takeshita, H. T.; Tanaka, H.; Kuriyama, N.; Sakai, T.; Uehara, I.; Haruta, M. Hydriding properties of LaNi₃ and CaNi₃ and their substitutes with PuNi₃-type structure. J. Alloy. Compd., 2000, 302, 304–313. https://doi.org/10.1016/S0925-8388(00)00694-0.
- (17) Zhang, X.; Yin, W.; Chai, Y.; Zhao, M. Structure and electrochemical characteristics of RENi₃ alloy. *Mater. Sci. Eng. B*, **2005**, *117*, 123-128. https://doi.org/10.1016/j.mseb.2004.11.017.
- (18) Liang, G.; Schulz, R. Phase structures and hydrogen storage properties of Ca-Mg-Ni alloys prepared by mechanical alloying. J. Alloy. Compd., 2003, 356-357, 612-616. https://doi.org/10.1016/S0925-8388(02)01285-9.
- (19) Kadir, K.; Sakai, T.; Uehara, I. Structural investigation and hydrogen capacity of YMg₂Ni₉ and (Y_{0.5}Ca_{0.5})(MgCa)Ni₉: new phases in the AB₂C₉ system isostructural with LaMg₂Ni₉. J. Alloy. Compd., 1999, 287, 264–270. https://doi.org/10.1016/S0925-8388(99)00041-9.
- (20) Sia, T. Z.; Zhang, Q. A.; Pang, G.; Liu, D. M.; Liu, N. Structural characteristics and hydrogen storage properties of $Ca_{3.0-x}Mg_xNi_9$ (x=0.5, 1.0, 1.5 and 2.0) alloys. *Int. J. Hydrogen Energy*, **2009**, 34, 1483–1488. https://doi.org/10.1016/j.ijhydene.2008.11.051.

- (21) Kresse, G.; Hafner, J. Ab Initio Molecular Dynamics for Liquid Metals. *Phys. Rev.* B **1993**, 47, 558. https://doi.org/10.1103/PhysRevB.47.558.
- (22) Kresse, G.; Furthmüller, J. Efficiency of Ab-Initio Total Energy Calculations for Metals and Semiconductors Using a Plane-Wave Basis Set. Comput. Mater. Sci. 1996, 6, 15–50. https://doi.org/10.1016/0927-0256(96)00008-0.
- (23) Kresse, G.; Furthmüller, J. Efficient Iterative Schemes for Ab-Initio Total-Energy Calculations Using a Plane-Wave Basis Set. Phys. Rev. B 1996, 54, 11169. https://doi.org/10.1103/PhysRevB.54.11169.
- (24) Perdew, J. P.; Burke, K.; Ernzerhof, M. Generalized Gradient Approximation Made Simple. Phys. Rev. Lett. 1996, 77, 3865–3868. https://doi.org/10.1103/PhysRevLett.77.3865.
- (25) Ebert, H.; et al. The Munich SPR-KKR Package, version 8.6. https://www.ebert.cup.uni-muenchen.de/sprkkr8/licenses (2022).
- (26) Ebert, H.; Ködderitzsch, D.; Minár, J. Calculating Condensed Matter Properties Using the KKR-Green's Function Method-Recent Developments and Applications. Rep. Prog. Phys. 2011, 74, 096501. https://doi.org/10.1088/0034-4885/74/9/096501.
- (27) Liechtenstein, A. I.; Katsnelson, M. I.; Antropov, V. P. et al., Local spin density functional approach to the theory of exchange interactions in ferromagnetic metals and alloys. J. Magn. Magn. Mater. 1987, 67, 65–74. https://doi.org/10.1016/0304-8853(87)90721-9.
- (28) Tran, H. B.; Momida, H.; Matsushita, Y.; Sato, K.; Makino, Y.; Shirai, K.; Oguchi, T. Effect of Magnetocrystalline Anisotropy on Magnetocaloric Properties of an AlFe₂B₂ Compound. Phys. Rev. B 2022, 105, 134402. https://doi.org/10.1103/PhysRevB.105.134402.

(29) Tran, H. B.; Momida, H.; Matsushita, Y.; Shirai, K.; Oguchi, T. Insight into Anisotropic Magnetocaloric Effect of CrI₃. *Acta Mater.* **2022**, *231*, 117851. https://doi.org/10.1016/j.actamat.2022.117851.